On-Chip Light Polarization Management by Mapping the Polarization Information to Phase Shift

Qingzhong Deng,* Ming Jin, Jun Qin, Pengfei Sun, Haowen Shu, Cheng Ju, Pieter Neutens, Zihan Tao, Peiqi Zhou, Bo Wang, Yuansheng Tao, Xuguang Zhang, Jingbo Shi, Bowen Bai, Lu Liu, Xi Xiao, Pol Van Dorpe, Xingjun Wang,* and Zhiping Zhou*

The comprehensive management of light polarization states has significantly advanced various fields into a new era. With the advent of photonic integration, there has been a persistent desire to replace the bulky optical components with compact chip-scale circuits. Nonetheless, the complete integration of polarization-dependent systems has not yet been accomplished due to the absence of a mature polarization management scheme that possesses a tiny form factor and high foundry process compatibility meanwhile maintaining low operation complexity. Here, to overcome these limitations a novel concept called polarization phase mapping, which encodes the information between the light polarization in one waveguide and the relative light phase shift in another two waveguides, is proposed. With this bi-directional mapping approach, the fundamental basis of polarization management has shifted from polarization adjustment to phase regulation. All essential polarization-related functions including synthesizing, stabilizing, measuring, rotating, splitting, and mixing are demonstrated with the standard process in foundries. The size of the polarization rotating unit is pushed down to a few light wavelengths while keeping a competitive performance. Moreover, the proposed concept can be readily applied to other integrated photonics platforms. It is expected to unlock new opportunities for complex polarization-related applications.

1. Introduction

Over the past decades, the pursuit of enhancing the capacity, accuracy, and sensitivity of optical systems has led to significant advancements in the management of light polarization with wide-ranging applications. For example, the utilization of polarization division multiplexing technique has improved the spectrum efficiency of communication systems,[1–3] monitoring the polarization of regular optical telecommunication channels can sense the seismic waves and detect submarine earthquakes,[4] controlling the polarizations in nanoparticle size spectrometry system has pushed the resolution down to 10-nm-level,[5–7] and polarization imaging has enabled the reconstruction of specular surfaces.[8,9] Besides harnessing polarization to improve system performance, recent advances in integrated photonic chips have allowed for the replacement of bulky optical components, enabling

Q. Deng, M. Jin, P. Sun, H. Shu, Z. Tao, B. Wang, Y. Tao, X. Zhang, J. Shi, B. Bai, L. Liu, X. Wang, Z. Zhou
State Key Laboratory of Advanced Optical Communication Systems and Networks
School of Electronics
Peking University
Beijing 100871, China
E-mail: qingzhong.deng@imec.be; xjwang@pku.edu.cn; zjzhou@pku.edu.cn

Q. Deng, P. Neutens, P. Van Dorpe
imec
Leuven B-3001, Belgium

Q. Deng, P. Van Dorpe
Department of Physics and Astronomy
Research unit Quantum Solid-State Physics
KU Leuven, Leuven B-3001, Belgium

M. Jin, H. Shu, Z. Tao, B. Wang, Y. Tao, X. Zhang, J. Shi, B. Bai, X. Wang
Frontier Science Center for Nano-optoelectronics
Peking University
Beijing 100871, China

J. Qin
Key Laboratory of Information and Communication Systems
Ministry of Information Industry
Beijing Information Science and Technology University
Beijing 100192, China

H. Shu, X. Wang
Peng Cheng Laboratory
Shenzhen 518055, China

the implementation of versatile optoelectronic functionalities in a scalable and cost-effective manner.[10,11] However, despite the tremendous progress achieved in integrated optical systems, the majority of polarization-relevant chip-level demonstrations require off-chip apparatus for polarization manipulation.[3,12,13] The lack of omnipotent integrated polarization management scheme, possessing a minimal form factor while keeping competitive performance and foundry process compatibility, has posed difficulties in the realization of fully integrated polarization-dependent optical systems.[14–16]

For typical waveguide-based polarization managements, a polarization rotating unit, bridging the two fundamental polarizations quasi transverse electric (TE) and quasi transverse magnetic (TM), are indispensable. The essence of the rotation in a waveguide is symmetry breaking. Conventionally, the asymmetric directional coupling[17–28] and $TM_0 - TE_1$ mode evolution[29–54] concepts are widely employed for symmetry breaking owing to their fabrication-friendly nature. However, they are not extensively accepted as the ideal choices in dense integration due to their hundreds-of-micrometer level size. The meta-structured waveguides[22,55–58] and some two-modes beating[59–65] based designs can result in compact devices but encounter insurmountable challenges in the wafer-level fabrication difficulties posed by CMOS-incompatible material stacks[22,55–60,62,63,65] or a small feature size.[22,55–58,61,64] Moreover, the two-modes beating and the $TM_0 - TE_0$ mode evolution schemes rotate both TE and TM input to the other irrepressibly. This is bound to require extra polarization beam splitter (PBS) for most applications, which leads to increased complexity.[66] On this basis, most polarization management implementations, including polarization synthesizers,[14,36,37,47,48,53,67,68] analyzers,[14,39,50] and stabilizers,[14,40,42] work on the same principle that first rotating the input polarizations into desired one and then connecting to a few cascaded couplers or Mach–Zehnder interferometers, which are relatively complicated and even at a mm-level footprint. The development of the polarization-sensitive optical system towards full and massively parallel integration is greatly hindered by the absence of a simple, compact, and handy polarization manipulating scheme.

Here, we propose a novel concept named polarization phase mapping to achieve comprehensive on-chip polarization management in simple architectures. By mapping the information between the light polarization in one waveguide and the relative light phase shift in another two waveguides, instead of manipulating the polarization state of one beam, the pivotal foundation of polarization management has been changed from ticklish polarization conversion to tractable phase regulation. The polarization phase mapping is fundamentally a blend of two-modes beating and mode evolution. The TM input is converted to two TE beams with π phase difference by two modes beating after propagating half beating length. The TE input, governed by the mode evolution between even symmetric modes, evolves to two TE beams with zero phase difference regardless the propagation length. The basic device based on this concept is named as polarization-phase mapper (PPM). We report the first PPM by using a simple partially etched slot (PE-slot) waveguide, which pushes down the half beating length to a few light wavelengths (5.42 μm for 1.55 μm light) while keeping compatibility with the standard processes in silicon photonics foundries. The PPM makes a lot of polarization related applications easy to implement. As a proof of concept, a polarization rotator-splitter (PRS), a dual-polarization coherent receiver, a polarization synthesizer, a polarization analyzer, and a polarization stabilizer are demonstrated, all of which exhibit competitive performance. Furthermore, a dual-polarization 90° optical hybrid is constructed using the PPM and the PRS, which is deployed for the first time in a real-time dual polarization coherent communication system. Meanwhile, a monolithic optical coherent receiver is realized by bonding the hybrid with on-chip balanced photodetectors, achieving coherent detection of quadrature phase shift keying (QPSK) and 16-ary quadrature amplitude modulation (16QAM) at the speed of $\geq$ 100 Gbps in an off-line demonstration.

2. Results

2.1. PPM Working Concept

The PPM consists of a multimode interference (MMI) based mode converter and a partially etched slot (PE-slot) waveguide as shown in **Figure 1a**. To ease the fabrication, the material stacks and the structure parameters are chosen based on the standard process in common commercial silicon photonics foundries. The material stacks are the silicon-on-insulator (SOI) with silicon oxide as the upper cladding. The PE-slot waveguide (Figure 1b inset) is the kernel of the PPM. The PE-slot waveguide is bilaterally symmetric with the waveguide thickness H = 220 nm, the slot width W_s = 200 nm and the slot etching depth H_s = 150 nm. The waveguide width W is the free parameter to be optimized. To connect the PE-slot waveguide with the MMI mode converter and the output strip waveguides, linear tapers are used to adapt W while the other parameters are kept as constants. Compared to traditional slot waveguide (Figure 1c inset), the only difference in PE-slot waveguide is the partial etching in the slot. However, this simple structural distinction has made the waveguide characteristics dramatically different. The PE-slot and slot waveguide mode analysis are presented in Figure 1b,c, respectively (see Note S2, Supporting Information, for the optical field distributions). Both waveguides have three eigenmodes when W is between 700 and 750 nm. In PE-slot waveguide, TE_0^{pe} is an even symmetric TE mode while EM_1^{pe} and EM_2^{pe} are hybridized in polarization. There is neither odd symmetric TE mode nor TM polarized mode. On the contrary, the eigenmodes of the slot waveguide are either TE or TM polarized. TE_0^{slot} is an even symmetric TE mode, TE_1^{slot} is an odd symmetric TE mode, and TM_0^{slot} is an

C. Ju
College of Electronic Information
Qingdao University
Qingdao 266071, China
P. Zhou, X. Xiao
National Information Optoelectronics Innovation Center
Wuhan 430074, China
X. Xiao
State Key Laboratory of Optical Communication Technologies and Networks
China Information and Communication Technologies Group Corporation (CICT)
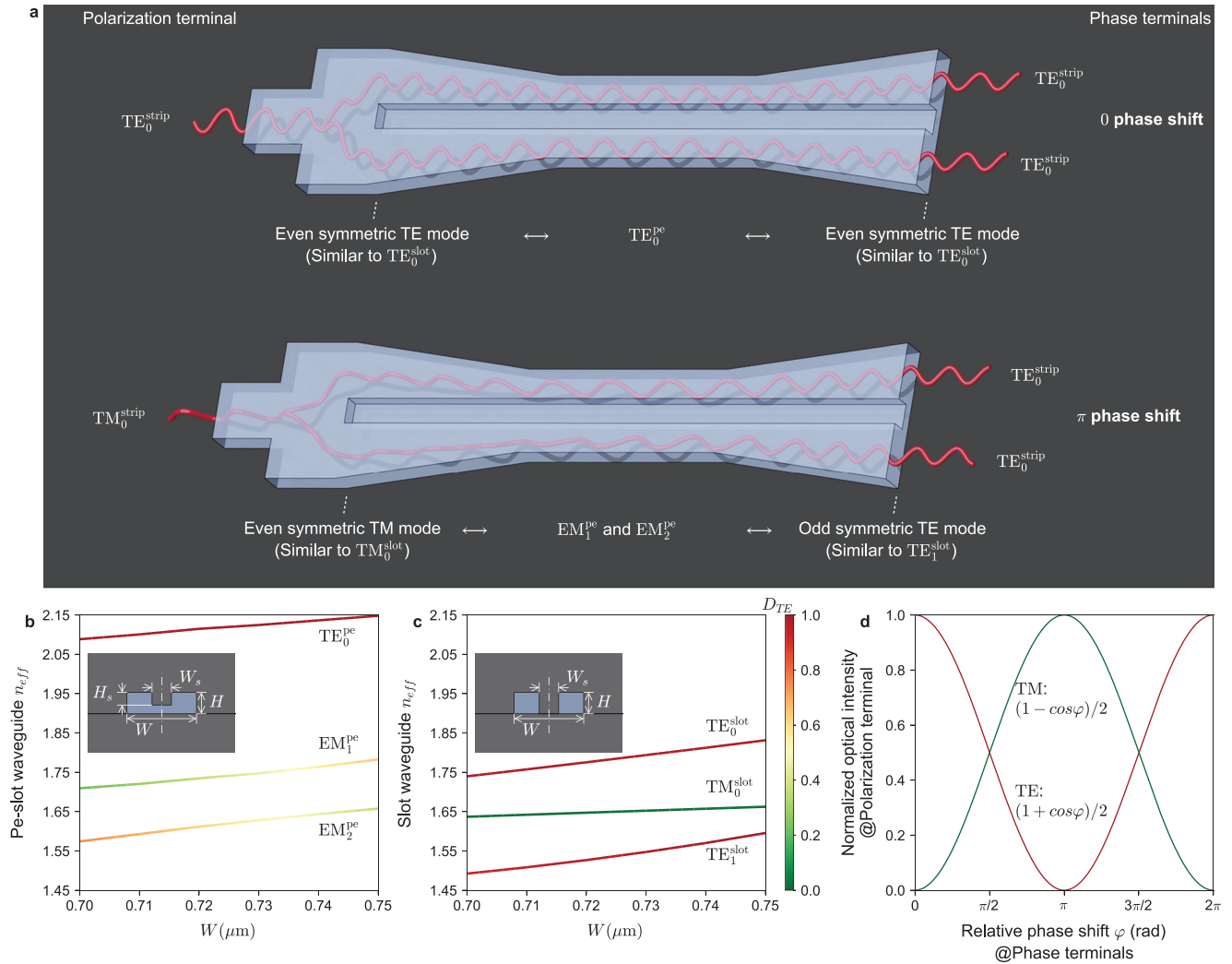Wuhan 430074, China

2300501 (2 of 12)

ADVANCED
SCIENCE NEWS

www.advancedsciencenews.com

LASER
& PHOTONICS
REVIEWS

www.lpr-journal.org

Figure 1. The PE-slot waveguide based PPM. a) The schematics of the PPM. b,c) The effective refractive index (n_{eff}) of the PE-slot (b) and slot (c) waveguide. The insets are the corresponding waveguide cross-sections. The colors of the curves represent the degree of TE-polarized (D_{TE}). The closer D_{TE} is to 1 (0), the more the mode polarization is similar to TE (TM). See Note S1, Supporting Information, for the definition of D_{TE}. The superscripts of the mode names are used to indicate the waveguide type, pe: PE-slot waveguide, slot: slot waveguide, strip: strip waveguide. d) The theoretical ideal relationship between the light polarization at the PPM polarization terminal and the relative phase shift at the PPM phase terminals.

even symmetric TM mode. When the light injects to the PPM from the polarization terminal, the TE_0^{strip} input is converted to an even symmetric TE mode (similar to TE_0^{slot}) while the TM_0^{strip} input is converted to an even symmetric TM mode (similar to TM_0^{slot}) by the MMI mode converter.[69] Then, the TE_0^{slot}-like mode is converted to TE_0^{pe} in the PE-slot waveguide since both of them are even symmetric TE modes. The light keeps as an even symmetric TE mode which is equivalent to two TE_0^{strip} beams with 0 relative phase shift. The TM_0^{slot}-like mode is decomposed into the superposition of EM_1^{pe} and EM_2^{pe} because the PE-slot waveguide can not support a TM mode. Similarly, a TE_1^{slot}-like mode in the PE-slot waveguide will be also decomposed into the superposition of EM_1^{pe} and EM_2^{pe} because it can not support odd symmetric TE mode neither. When the PE-slot waveguide width W is chosen properly, TM_0^{slot}-like and TE_1^{slot}-like mode can have the same superposition coefficient magnitude but with π phase difference

(see Note S3, Supporting Information, for the mode expansion analysis). On the other hand, EM_1^{pe} and EM_2^{pe} have different effective refractive index (n_{eff}^{EM1} and n_{eff}^{EM2}) as shown in Figure 1b. The two modes will accumulate π phase difference after the propagation length of $\lambda/2(n_{eff}^{EM1} - n_{eff}^{EM2})$, where λ is the light wavelength, which means the TM_0^{slot}-like mode is converted to the TE_1^{slot}-like mode. The TE_1^{slot}-like mode is an odd symmetric TE mode that is equivalent to two TE_0^{strip} beams with π relative phase shift. This is how the PPM maps the polarization information into the relative phase shift (see Note S13, Supporting Information, for more numerical analysis). Obviously, the PPM is reciprocal. When two TE_0^{strip} beams inject from the phase terminals, the output light from the polarization terminal will be TE (TM) polarized if the input relative phase shift is 0 (π). In general cases, the intensity of the two output polarizations will be in a cosinusoidal relationship with the input relative phase shift as shown in Figure 1d.
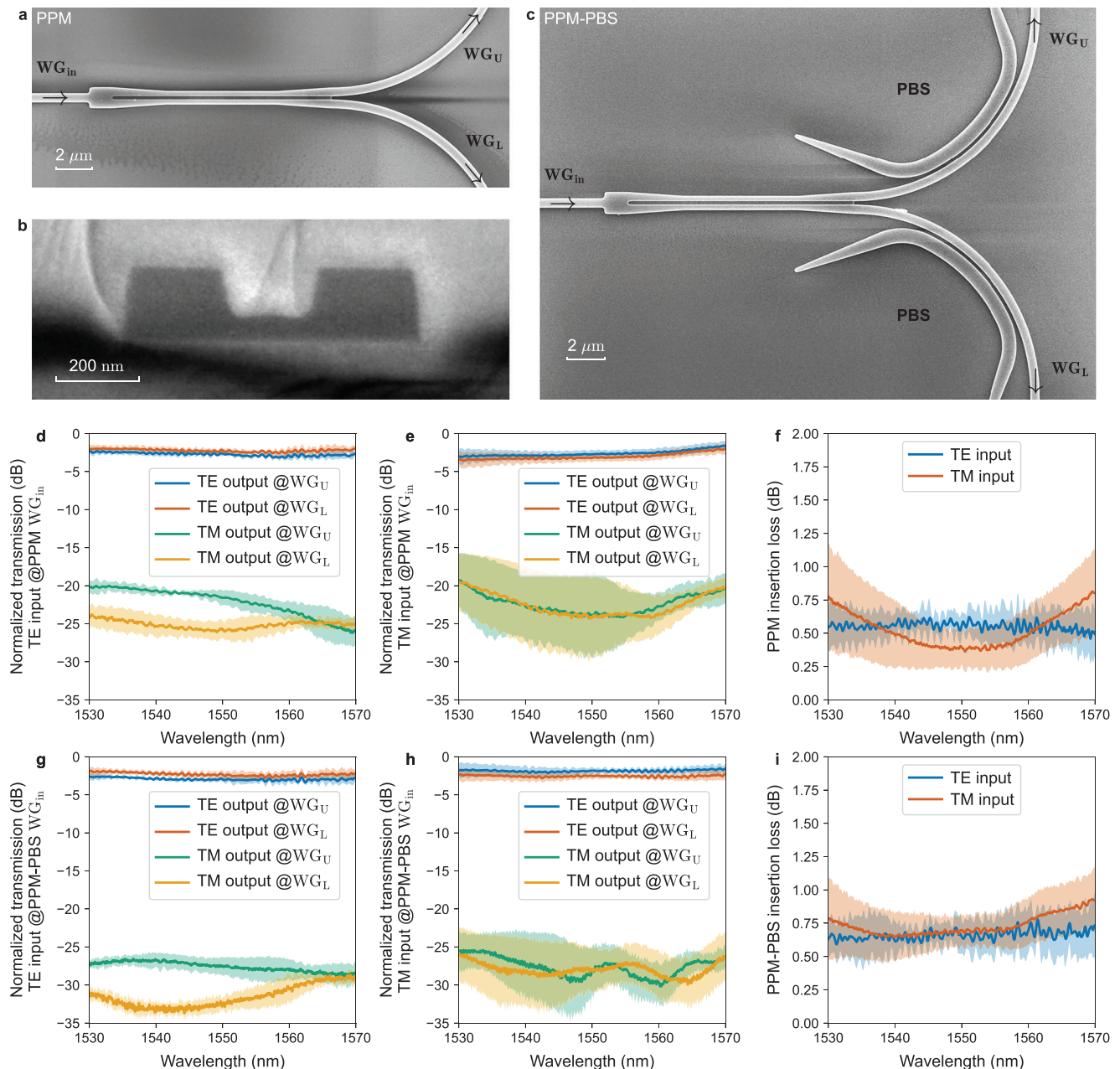
ADVANCED
SCIENCE NEWS
www.advancedsciencenews.com

LASER
& PHOTONICS
REVIEWS

www.lpr-journal.org

Figure 2. The PPM performance characterization. a–c) The scanning electron microscopes (SEMs): the top-view of the PPM (a), the cross-section view of the PE-slot waveguide (b), and the top-view of the PPM cascaded with a PBS on each output waveguide (PPM-PBS) (c). The PPM and the PPM-PBS top-view SEM are taken with the SiO_2 top cladding removed. The nominal dimensions of the PPM: the MMI width is 1.1 μm; the MMI length is 1.2 μm; the taper length from the MMI to the PE-slot waveguide is 3 μm; the PE-slot waveguide width is 0.71 μm; the PE-slot waveguide length is 6.2 μm; the taper length from the PE-slot waveguide to the output strip waveguides is 3 μm; and the width of the input (WG_{in}) and output (WG_U and WG_L) strip waveguides is 0.45 μm. d,e,g,h) The measured transmission spectra of the PPM (d,e) and PPM-PBS (g,h) with TE (d,g) and TM (e,h) input. f,i) The measured insertion loss of the PPM (f) and PPM-PBS (i). The curves are the mean values while the bands with light colors are the standard deviations of the measurements for five dies.

The scanning electron micrograph (SEM) of the fabricated PPM is shown in **Figure 2a**, and the cross-section view of the PE-slot waveguide is shown in Figure 2b. The footprint of the PPM is 1.1×13.4 μm². As indicated by the measured transmission spectra (Figure 2d,e), no matter the input polarization from WG_{in} is TE or TM, the dominant outputs from WG_U and WG_L

are TE-polarized and have a similar intensity. Within C-band (the wavelength range of 1530–1565 nm), the measured polarization extinction ratio (PER) is better than 17.6 ± 1.0 dB for TE input and 16.0 ± 4.8 dB for TM input; the highest PER is 22.0 ± 2.6 dB for TE input and 21.0 ± 5.8 dB for TM input. The insertion losses (IL) are plotted in Figure 2f, which are measured with four

2300501 (4 of 12)

**ADVANCED
SCIENCE NEWS**

www.advancedsciencenews.com
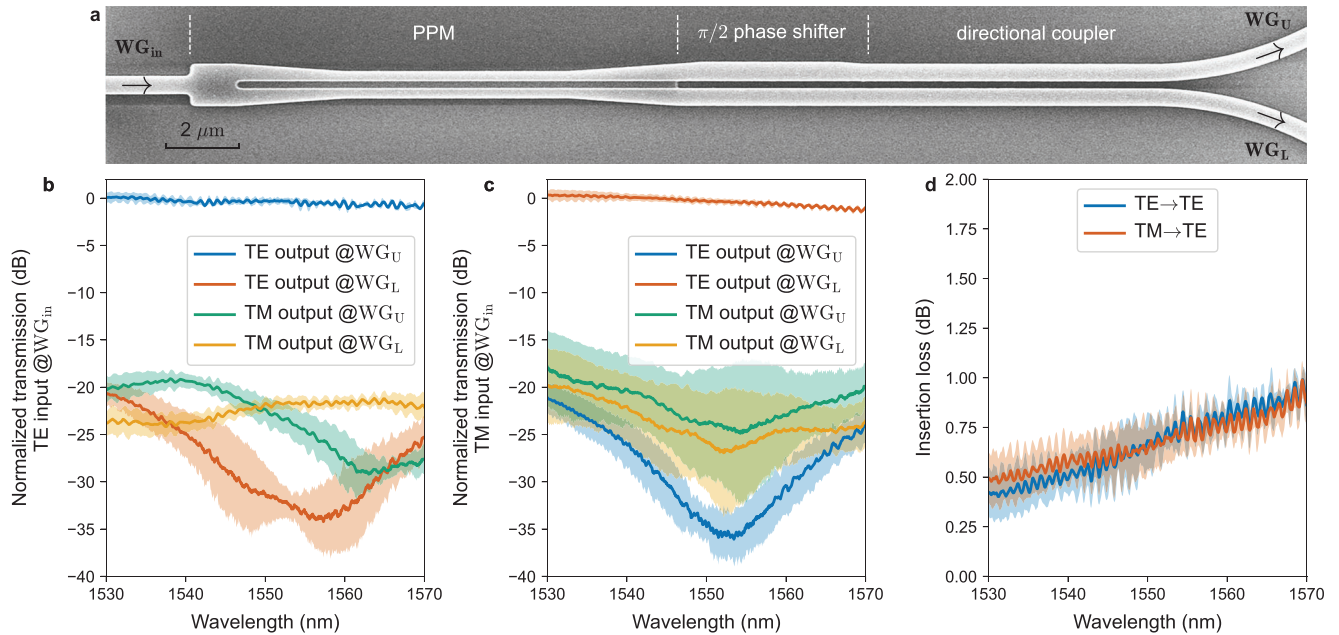
**LASER
& PHOTONICS
REVIEWS**

www.lpr-journal.org

Figure 3. The PRS implemented with the PPM. a) The top-view SEM of the fabricated PRS. The SEM is taken with the SiO$_2$ top cladding removed. The nominal dimensions of the PRS. The right end of the PPM consists of two waveguides with the width of 0.45 µm; the upper waveguide is widen to 0.5 µm to provide π/2 relative phase shift; the length of the widened waveguide is 3.76 µm; the length of the tapers converting the two waveguide width is 0.70 µm; The straight length in the directional coupler is 8.0 µm; The bending radius is 10 µm in the output bends. b,c) The measured transmission spectra with TE (b) and TM (c) input. d) The measured insertion loss. The curves are the mean values while the bands with light colors are the standard deviations of the measurements for five dies.

identical PPMs cascaded (see Note S4, Supporting Information, for the measurement details). Within C-band, the IL is better than 0.62 ± 0.11 dB for TE input and 0.78 ± 0.49 dB for TM input; the lowest IL is 0.49 ± 0.17 dB for TE input and 0.36 ± 0.15 dB for TM input. The PER can be further improved by cascading a PBS on each output waveguide (Figure 2c). Within C-band, the PER is better than 23.7 ± 1.2 dB for TE input and 23.5 ± 4.4 dB for TM input; the highest PER is 25.6 ± 1.7 dB for TE input and 26.8 ± 3.4 dB for TM input (Figure 2g,h). The IL is better than 0.78 ± 0.12 dB for TE input and 0.85 ± 0.20 dB for TM input; the lowest IL is 0.59 ± 0.14 dB for TE input and 0.64 ± 0.18 dB for TM input (Figure 2i). These measurements have verified the PPM concept that converts both TE and TM light into two beams of TE light beams with similar intensities. In the following sections, a few functional devices are constructed to demonstrate its potential versatile applications.

2.2. PPM Based Polarization Rotator-Splitter

A polarization rotator-splitter (PRS) is one of the most fundamental components for polarization management and applications. The functionality of a PRS is to separate the optical power carried by TE and TM polarization in one waveguide into two waveguides. The light beams in both output waveguides are TE polarized. A PRS can be achieved by cascading the PPM with a π/2 phase shifter and a directional coupler as shown in **Figure 3a** wherein the π/2 phase shifter is implemented by varying the waveguide width. The PPM converts the TE_0^{strip} (TM_0^{strip}) input into two equal-intensity TE_0^{strip} beams with a relative phase shift

of 0 (π). Then the π/2 phase shifter makes the phase difference of the two beams to be $\pm\pi/2$, respectively. Finally, the directional coupler combines the light originally from TE_0^{strip} (TM_0^{strip}) input to WG_U (WG_L) output waveguide as TE_0^{strip}. The measured transmission spectra are plotted in Figure 3b,c, and the IL is plotted in Figure 3d. Within C-band, the measured PER is better than 18.8 ± 1.3 dB for TE input and 18.2 ± 4.5 dB for TM input; the highest PER is 21.9 ± 1.0 dB for TE input and 24.4 ± 8.0 dB for TM input. The IL is better than 0.90 ± 0.07 dB for TE input and 0.84 ± 0.10 for TM input; the lowest IL is 0.40 ± 0.11 dB for TE input and 0.47 ± 0.13 dB for TM input (See Note S4, Supporting Information, for the measurement details). The PRS shows stronger wavelength dependency than the PPM, which is caused by the directional coupler. It can be improved by replacing the directional coupler with a broadband design such as ref. [70].

2.3. PPM Based Polarization Synthesizer

The key functionalities required for polarization management include polarization synthesizing, analyzing, and stabilizing. All of them can be easily implemented with the PPM as shown in **Figure 4**. The PPM maps the polarization of one light beam to the relative phase shift of two TE light beams and vice versa. It is straight-forward to construct a polarization synthesizer as Figure 4a. The input TE light is splitted into two waveguides with the same intensity. A phase shifter is cascaded on one waveguide to control the relative phase shift, and then the PPM is used to convert the relative phase shift to the polarization of the output.
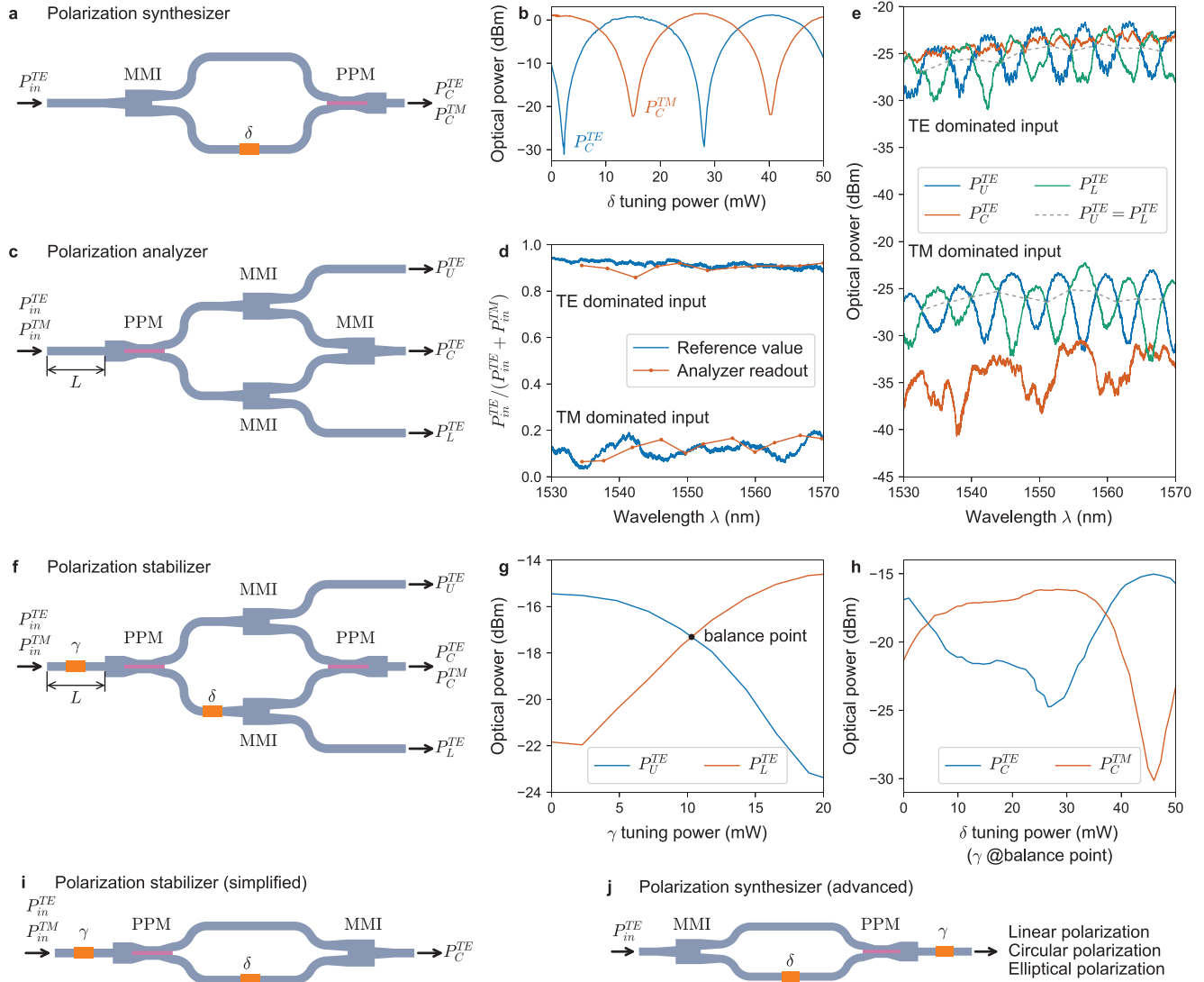
Figure 4. Proof-of-concept experiments of the PPM based polarization management. a,b) The schematics (a) and the experimental data (b) of the polarization synthesizer. c–e) The schematics (c), the R_{in}^{TE} readout (d) and the output spectra (e) of the polarization analyzer. f–h) The schematics (f), the γ phase shift (g), and δ phase shift (h) of the polarization stabilizer. i) The schematics of the simplified polarization stabilizer. j) The schematics of the advanced polarization synthesizer that is constructed by swapping the input and output of the advanced polarization synthesizer. P represents the input or output optical power with its superscript denotes the polarization, TE or TM. The subscript denotes the waveguide position: in, the input waveguide; U, the upper output waveguide; C, the central output waveguide; L, the lower output waveguide. γ and δ are the phase shifts in the phase shifters. L is the length of the input waveguide.

In ideal situation, the output light intensities of the two polarizations can be expressed as

$$\begin{cases} P_C^{TE} = P_{in}^{TE}(1 + \cos\varphi)/2 \\ P_C^{TM} = P_{in}^{TE}(1 - \cos\varphi)/2 \\ \varphi = \varphi_0 + \delta \end{cases} \quad (1)$$

where φ_0 denotes the initial phase difference of the light in the two waveguides, and δ denotes the phase shift by the phase shifter. The polarization synthesizer is verified with some preliminary results as shown in Figure 4b (see Note S9, Supporting Information). A thermo-optic phase shifter is used to control the

relative phase shift δ. The output intensities of the two polarizations vary in a sinusoidal like relationship with the tuning power. When one extra phase shifter is placed after the PPM (Figure 4j), the relative intensity of the output TM_0^{strip} and TE_0^{strip} is controlled by δ while the relative phase is controlled by γ. It can be used to synthesize more advance polarizations, such as right-handed or left-handed circular polarization, and elliptical polarization.

2.4. PPM Based Polarization Analyzer

The PPM maps both TM_0^{strip} and TE_0^{strip} input as two equal-intensity TE_0^{strip} outputs. Therefore, interference can be observed

2300501 (6 of 12)

ADVANCED
SCIENCE NEWS

www.advancedsciencenews.com

LASER
& PHOTONICS
REVIEWS

www.lpr-journal.org

at the outputs when the input is a mixture of TM_0^{strip} and TE_0^{strip}. In ideal situation, the output light intensities P_U^{TE} and P_L^{TE}, from WG_U and WG_L (Figure 2a) respectively, can be expressed as

$$
\begin{cases}
P_U^{TE} = (P_{in}^{TE} + P_{in}^{TM} + 2\sqrt{P_{in}^{TE} P_{in}^{TM}} \cos\phi)/2 \\
P_L^{TE} = (P_{in}^{TE} + P_{in}^{TM} - 2\sqrt{P_{in}^{TE} P_{in}^{TM}} \cos\phi)/2 \\
\phi = \phi_0 + 2\pi(n_{eff}^{TE} - n_{eff}^{TM})L/\lambda
\end{cases}
\tag{2}
$$

where P_{in}^{TE} and P_{in}^{TM} are the intensities of the TE and TM input respectively, ϕ_0 denotes the initial phase difference between the TE and TM input, n_{eff}^{TE} and n_{eff}^{TM} denote the effective refractive index of the TE and TM light in the input waveguide, and L is the length of the input waveguide before entering the PPM. This feature can be used to construct a polarization analyzer. According to Equation (2), the extinction ratio (ER) between the constructive peak and the adjacent destructive peak in P_U^{TE} or P_L^{TE} can be expressed as

$$
ER = 20 \log \left| \frac{\sqrt{P_{in}^{TE}} + \sqrt{P_{in}^{TM}}}{\sqrt{P_{in}^{TE}} - \sqrt{P_{in}^{TM}}} \right|
\tag{3}
$$

The TE_0^{strip} input power ratio (R_{in}^{TE}) can be derived as

$$
R_{in}^{TE} \doteq \frac{P_{in}^{TE}}{P_{in}^{TE} + P_{in}^{TM}} =
\begin{cases}
\frac{(r+1)^2}{2(r^2+1)}, & \text{if } P_{in}^{TE} \geq P_{in}^{TM}; \\
\frac{(r-1)^2}{2(r^2+1)}, & \text{if } P_{in}^{TE} < P_{in}^{TM}; \quad r = 10^{ER/20}
\end{cases}
\tag{4}
$$

The same ER results in two R_{in}^{TE} values. To identify which value corresponds to the real input, half of the light from each output of the PPM are collected by one symmetric 2×1 MMI combiner as shown in Figure 4c. In ideal situation, the output intensities can be expressed as

$$
\begin{cases}
P_U^{TE} = (P_{in}^{TE} + P_{in}^{TM} + 2\sqrt{P_{in}^{TE} P_{in}^{TM}} \cos\phi)/4 \\
P_C^{TE} = P_{in}^{TE}/2 \\
P_L^{TE} = (P_{in}^{TE} + P_{in}^{TM} - 2\sqrt{P_{in}^{TE} P_{in}^{TM}} \cos\phi)/4 \\
\phi = \phi_0 + 2\pi(n_{eff}^{TE} - n_{eff}^{TM})L/\lambda
\end{cases}
\tag{5}
$$

P_U^{TE} and P_L^{TE} oscillate around $(P_{in}^{TE} + P_{in}^{TM})/4$ with the change of the wavelength, while P_C^{TE} is a signpost for TE_0^{strip} input. When P_C^{TE} is higher than the oscillation baseline of P_U^{TE} and P_L^{TE}, it means $P_{in}^{TE} \geq P_{in}^{TM}$ in the input and vice versa. The measured spectra (Figure 4e) agree well with the theoretical analysis, where P_U^{TE} and P_L^{TE} show reciprocal sinusoidal oscillations. P_C^{TE} is lower than the oscillation baseline (the gray dashed lines in Figure 4e) with TM dominant input, and higher with TE dominate input. The R_{in}^{TE} readout from the spectra is plotted in Figure 4d, which matches well with the reference value (see Note S10, Supporting Information, for the experiment details). In this demonstration, the ER is read out from the spectra. To analyze the input polarization with single wavelength, the ER can be read out by cascading

a phase shifter at the input waveguide (same as phase shifter γ in Figure 4f). P_U^{TE} and P_L^{TE} intensities will change with the phase shifting. The ER can be calculated with the maximum and minimum output intensity from P_U^{TE} or P_L^{TE}.

2.5. PPM Based Polarization Stabilizer

A polarization stabilizer is the device to maintain the output polarization to a specified state no matter what the input polarization is. Extended from the polarization analyzer, the PPM can be used to construct a polarization stabilizer as shown in Figure 4f. Two controllable phase shifters are inserted in the input waveguide and one of the PPM output waveguide respectively, and the MMI combiner in Figure 4c is replaced by a PPM. The first PPM can output two equal-intensity TE_0^{strip} beams no matter what the input polarization state is if ϕ is tuned to $\pi/2$, as indicated by Equation (5). Therefore, tuning γ to make $P_U^{TE} = P_L^{TE}$ is the first step for the stabilizer. The experimental results are shown in Figure 4g. Then, tuning δ to control the relative phase of the two beams reaching the second PPM can manipulate the output polarization state (similar to Equation (1)), as shown in Figure 4h. Note that the MMI splitters are only used to split part of the light to monitor the intensity. They are not necessary to be 50:50 splitters. In practice, the splitters can be removed or replaced by an asymmetric splitter[71] to split a small portion of the power for monitoring so that most of the input power can be converted to the desired output polarizations. The polarization stabilizer in Figure 4f can output any specified combination of TM_0^{strip} and TE_0^{strip}. In most applications, the output is expected to be stabilized as TE polarized. The polarization stabilizer can be simplified as Figure 4i. When the output P_C^{TE} is maximized by tuning γ and δ, all the input light can be convert into TE output in ideal situation, that is, $P_C^{TE} = P_{in}^{TE} + P_{in}^{TM}$.

2.6. PPM Based Optical Coherent Receiver

As verified in the polarization analyzer section, interference can be observed at the outputs when the input is a mixture of TM_0^{strip} and TE_0^{strip}. This feature can be exploited as a 180° optical hybrid if the two input polarizations are assigned as the signal and the local oscillator (LO), respectively in a coherent receiver.[44] The 180° hybridizing is originated from the mode symmetry of TE_0^{slot} (even symmetric) and TE_1^{slot} (odd symmetric) so that the hybridizing is robust and independent to ambient temperature fluctuations (see Note S5, Supporting Information). **Figure 5a** illustrates the system architecture[44] of the fabricated 90° optical dual-polarization (DP) hybrid, which is composed of four PPMs, a PBS, and a PPM-based PRS (see Note S6 and Figure S8, Supporting Information). The 90° phase difference between in-phase (I) and quadrature (Q) components is achieved through waveguide birefringence between the signal (TE_0^{strip}) and LO (TM_0^{strip}). The phase properties of the DP-hybrid are characterized through homodyne method (see Note S6, Supporting Information). According to the measured spectra of output ports (see Figure S9, Supporting Information), the phase deviations under different input mode is calculated in Figure 5b. The phase deviations between the ports are less than
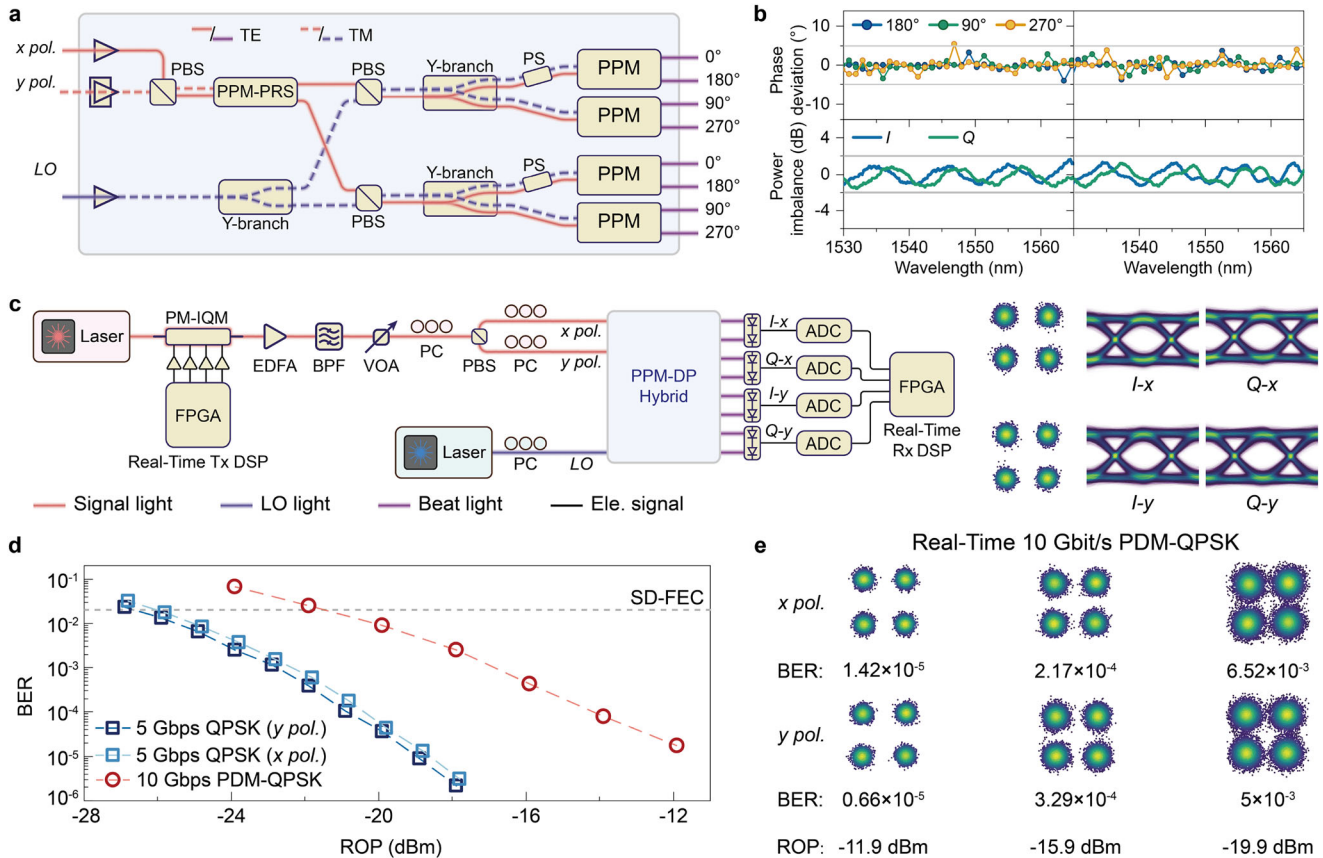
Figure 5. PPM based 90° optical dual-polarization hybrid and real-time coherent transmission. a) The schematic of the PPM based DP-hybrid. b) The measured phase deviation and power imbalance of the hybrid. c) The real-time coherent transmission system based on the DP-hybrid. Inset: Constellation diagrams and reconstructed eye diagrams of received QPSK signal with different input polarization in the real-time system. d) The measured BERs versus the received power for single polarization and polarization division multiplexing (PDM) QPSK signal. e) The constellation diagrams and corresponding BERs of the PDM-QPSK signal transmission under different received power in the real-time system.

5° in the entire C-band. The power imbalances, obtained through testing the transmissions of four output ports synchronously, are less than 2 dB in the C-band (Figure 5b). The phase deviations and power imbalances can be easily compensated by the digital signal-processing (DSP) for a coherent transmission system.

The DSP-based coherent optical communication systems are widely viewed as the most promising next generation long-haul optical transport systems. One of the biggest challenges in deploying these systems in network is the implementation of signal processors that are able to deal with signaling rates of a few tens of gigabits per second in real-time operation.[72] Compared to the offline systems which demodulating the signals by employing offline DSP after capturing the data, real-time coherent systems are more efficient, and more promising to be deployed in actual optical communication networks. To further verify the performance of the PPM-based hybrid, a real-time DP coherent transmission system which supported by field-programmable gate arrays (FPGA) is developed, as shown in Figure 5c (see Note S7, Supporting Information). By employing the PPM-based DP-hybrid shown in Figure 5a, we first implement single-polarization (SP) advanced modulation format reception at 1550 nm. As one of the most widely used modulation formats in coherent optical communications, QPSK signal is performed to detect by the optical

coherent receiver. After the SP-QPSK signal that generated by the PM-IQ modulator in the transmitter, it is sent into the optical coherent receiver for detection by one of the grating coupler (Figure 5a). After that, DP-QPSK signal reception is conducted. For the detection of DP-QPSK signal, it is achieved by sending two SP signals into the two grating couplers, respectively at the same time. The measured bit error rate (BER) and constellation diagrams at different ROPs for different situations are given in Figure 5d,e. The line rates of received data as 5 Gbps (SP-QPSK) and 10 Gbps (DP-QPSK) are achieved. All constellation diagrams for SP-QPSK and DP-QPSK show high-quality reception, of which the BERs are lower than the hard-decision forward error correction threshold (HD-FEC, 3.8×10^{-3}) at a ROP of -22 and -18 dBm, respectively. The slight performance difference between x pol. and y pol. is caused by the different coupling loss for TM and TE grating coupler.

Then, a monolithic optical coherent receiver is realized with PPM-based hybrid and on-chip germanium balanced photodetector (BPD) with 3 dB-bandwidth of 27 GHz (see Note S8, Supporting Information). Here, owing to the area limitation for optical packaging, only the SP-QPSK/16QAM signal can be coherently received by the PPM-based optical coherent receiver. The experimental setup and packaged optical coherent receiver are
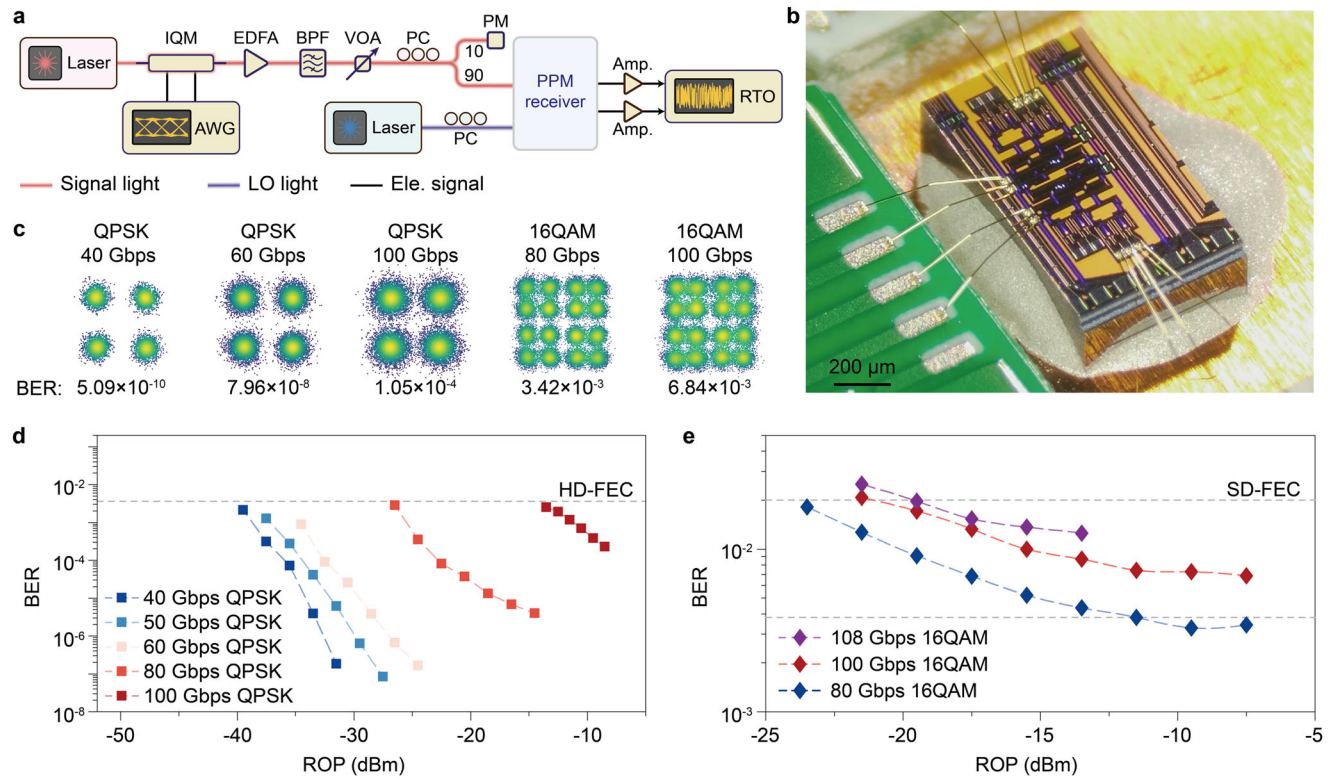
ADVANCED
SCIENCE NEWS

www.advancedsciencenews.com

LASER
& PHOTONICS
REVIEWS

www.lpr-journal.org

Figure 6. PPM based optical coherent receiver and off-line reception measurement. a) Measurement setup for the coherent detection. b) Optical microscopy image of the packaged monolithic coherent receiver. c) Constellation diagrams of received single-polarization QPSK/16QAM signal at different transmission rates. d,e) Measured BERs versus received optical power (ROP) of QPSK (d) and 16QAM (e) signals.

shown in **Figure 6**a,b. Figure 6c illustrates the measured constellation diagrams of QPSK (line rates of 40, 60, and 100 Gbps) and 16QAM (line rates of 80 and 100 Gbps) signals. The BERs of these received constellation diagrams are below the soft-decision forward error correction limit (SD-FEC, 2×10^{-2}). Even the data rate of QPSK signal reaches 100 Gbps, the BERs is still below the HD-FEC limit of 3.8×10^{-3}, suggesting our receiver has the ability to detect coherent signal with data rates exceeding 100 Gbps. As shown in Figure 6d,e, back-to-back BERs test curves are performed on QPSK/16QAM signals, reflecting the relationship between BER and signal light power at 7-dBm LO light. Moreover, by optimizing the optical I/O strategy and the bandwidth of BPD, the demonstrated receiver shall support coherent reception up to 200/400 Gbps or higher rates.

3. Discussion

In this article, a novel concept that encodes the information between the light polarization in one waveguide and the relative light phase shift in another two waveguides is proposed for on-chip light polarization management. With this bi-directional polarization phase information mapping, the pivotal foundation of polarization management has been changed from ticklish polarization conversion to tractable phase regulation. A PE-slot waveguide is proposed to implement this concept as a PPM with the size of a few light wavelengths only ($1.1 \times 13.4\ \mu m^2$ for 1.55 μm light) while keeping the fabrication compatibility with the standard process in all popular silicon photonics foundries (180

nm mask technology or more advanced). The waveguides with $TM_0 - TE_1$ mode evolution[35–37,43,44,46,49,53] can also be used to implement the proposed concept but with a much larger (> 3.6×) footprint (see Note S11, Supporting Information). Moreover, the footprint of the PE-slot waveguide based PPM can be further reduced. First, the length of each tapered PE-slot waveguides in the PPM is fixed to 3 μm which can be shortened to ≈ 2 μm without significantly increasing the loss.[69] Second, the slot width and etching depth are fixed to 200 and 150 nm, respectively. The PPM dimension is reduced to $1.1 \times 11.9\ \mu m^2$ when the etching depth is 130 nm (Figure S13, Supporting Information). If there are more freedom in choosing the slot width and etching depth, the PPM can be more compact (see Note S3, Supporting Information).

The PRS is the most widely researched component in polarization management and applications. As a benchmark, a PRS is constructed with the PPM. The comparison of the PPM-based PRS with the PRS experimentally demonstrated in literature[17,19,21–25,27–30,32,33,38,41,45,47–49,51,52,54] is listed in Note S12, Supporting Information. The PPM-based PRS shows good overall performance. Within C-band, the PER is better than 18.8 ± 1.3 dB for TE input and 18.2 ± 4.5 dB for TM input, and the highest PER is 21.9 ± 1.0 dB for TE input and 24.4 ± 8.0 dB for TM input. The IL is better than 0.90 ± 0.07 dB for TE input and 0.84 ± 0.10 for TM input, and the lowest IL is 0.40 ± 0.11 dB for TE input and 0.47 ± 0.13 dB for TM input. The footprint of the PPM-based PRS is $1.1 \times 26.6\ \mu m^2$ which is the smallest among the designs without any special fabrication requirements.

With the PPM and the PRS, a dual-polarization 90° optical hybrid has been constructed. The hybrid is successfully demonstrated in a 10 Gbps real-time DP-QPSK coherent communication system. To the best of our knowledge, this is the first demonstration of real-time coherent communication system by employing silicon DP-hybrid. Moreover, a monolithic optical coherent receiver is realized with the off-line system demonstration of ≥ 100 Gbps QPSK and 16QAM coherent detection. Since the transparency of PPM to signal baud rate, the transmission baud rate in the real-time system can be further promoted by adopting higher performance FPGAs and ADCs, or higher modulation formats. Similarly, the transmission baud rate in the off-line system demonstration can be improved by utilizing higher bandwidth BPD and optimizing the packaging.

The PPM provides a bidirectional mapping between the light polarization and phase shift. Combining the PPM with the state-of-the-art light phase shift makes a lot of polarization related applications easy to implement. In addition to the PRS and the coherent receivers, a polarization synthesizer, a polarization analyzer, and a polarization stabilizer have been demonstrated as proof of concepts. The phase shift in the demonstrations is constructed as normal thermo-optic phase shifters but it is not the limitation of the PPM. The PPM adds no constraint for the applicable phase shifters. The PPM does not need any special material stacks or fabrication process, and it uses the common single-mode strip waveguide as the input and output ports. Therefore, all existing phase shifting techniques in silicon photonics can incorporate with the PPM to achieve some fancy characteristics. For example, combining with an electro-optic phase shifter[73] can result in super-fast polarization synthesizer and stabilizer with ten pico-seconds scale time delay and combining with the doped Si thermo-optic phase shifter[74] can achieve ultra-compact form factor. Moreover, the functionality of the PPM is fundamentally based on the optical confinement of the PE-slot waveguide. Besides the refractive index difference between the waveguide core and cladding, no other special material property is required. The PPM and its versatile applications can be extended easily to other working wavelengths and photonics integrated circuits platforms. As proof of concepts, the polarization synthesizer (Figure 4a,b) is implemented on imec SiN platform with visible light, the polarization analyzer (Figure 4c,e) and the polarization stabilizer (Figure 4f–h) are implemented for C-band wavelength on advanced micro foundry (AMF) SOI platform, while the others are implemented for C-band wavelength on CompoundTek SOI platform. It is expected that all polarization related on-chip applications, ranging from optical communication to quantum information to bio-sensing to holography and so on, can benefit from the bi-directional mapping of the light polarization and phase shift enabled by the proposed PPM.

4. Experimental Section

Optical Simulation: All simulations in this article were performed with full vector finite element method (FEM), while the refractive indices of Si and SiO$_2$ were set to 3.48 and 1.45, respectively, and the working wavelength was set to 1550 nm if not specified.

Real-Time Coherent Communication System: As shown in Figure 5c, the signal light inputting into the commercial PM-IQ modulator (Fujitsu

FTM7977HQ, which comprised a 3 dB coupler, two QPSK modulators, polarization rotator followed by the polarization beam combiner, and the built-in monitor PD chips for automatic bias control for the compensation system of DC-drift and other phenomena) was generated by a tunable laser at 1550 nm. One FPGA (Intel 10AX066, with 250k adaptive logic modules, 32 kbit read-only memory, and 312.5 MHz clock frequency digital signal processor) was employed to drive the PM-IQ modulator as electrical signal generator. In the FPGA, four binary data streams from a $2^{13} - 1$ (XI, XQ, YI, YQ, 8191 bits for each) pseudorandom binary sequence (PRBS) generator was encoded and then mapped onto a QPSK constellation. After the mapping, 3-tap pr-emphasis compensation was implemented to compensate for the insufficient frequency response of the transmitter.

After the modulation, the signal was amplified by the EDFA, then an optical bandpass filter (OBPF) was used to filter out the ASE (amplified spontaneous emission) noise. Before being injected into the grating coupler of the hybrid for detection, one PBS was employed to divide the signal into two branches. Before the PBS, a tunable attenuator was used to control the optical power, and a polarization controller was used to adjust the polarization state. Another tunable laser works as the LO, which entered the hybrid with optical power of 7 dBm. After the hybrid, four commercial BPDs were utilized to do the balanced detection. The generated electrical signals from the BPDs were read out with 4 ADCs (Teledyne EV8AQ160, with 2 GHz bandwidth, 5 GSa s^{-1} sampling rate and 8 bit resolution) and then real-time processed with another FPGA (Intel 10AX066). In this receiver side FPGA, the following digital signal processing operations were implemented (see Note S7, Supporting Information). IQ imbalance was first handled by using Gram–Schmidt orthogonalization.[75] After this, the waveform was re-sampled to twice the symbol rate. Then Gardner[76] clock recovery algorithm was adopted to estimate the timing offset between the real samples and the optimal sampling points. Then, CMA-based (constant modulus algorithm) 2 × 2 MIMO (multiple input multiple output) equalizer[77] was used for signal equalization and polarization demultiplexing. Following is the fourth power-based frequency offset estimator to compensate for relative phase drifts between the signal carrier and the local oscillator. Last, the residual phase noise was compensated by the V-V (Viterbi–Viterbi) carrier phase algorithm.[78]

The BER was calculated by comparing the bit sequence decoded from the received symbols after symbol-to-bit demapping with the originally transmitted one. All the steps were performed independently for each polarization.

Off-Line Coherent Communication System: Two independent RF signals with a length of a PRBS of $2^{10} - 1$ were generated from a 120 GSa s^{-1} arbitrary waveform generator (Keysight, M8194A). A root-raised-cosine (RRC) filter with $\alpha = 0.1$ was used for pulse shaping. The signal were sent into a commercial IQ transmitter (Coherent Solutions, with 40 GHz bandwidth), which transmitted the modulated signal with a power of −1 dBm. The signal was amplified through an EDFA, which was followed by a bandpass filter to suppress ASE noise. The amplified signal was received B2B and mixed with a local oscillator (Santec TSL-550) with 14 dBm output power in PPM-based optical coherent receiver. The output I- and Q-branch signals from on-chip BPD were coupled out through wire bonded PCB, which were amplified by a pair of linear amplifiers (SHF S807C). A four-channel real-time oscilloscope (Keysight UXR0594A, 59 GHz, 256 GSa s^{-1}) was used for data sampling. A series of digital signal processing (DSP) steps, including matched RRC filtering and adaptive equalization built in the vector signal analysis (Keysight) software, were used in the signal processing. The data were then measured by error vector magnitude (EVM) and BER. Here, the BER values were estimated from EVM assuming the signal was distorted by additive white Gaussian noise only.[79] 10% of the transmitted signal was monitored to estimate the received optical signal of on-chip BPD.

Supporting Information

Supporting Information is available from the Wiley Online Library or from the author.

Acknowledgements

Conflict of Interest

Z.Z. and Q.D. have applied for patent CN106990478B for on-chip polarization management. The other authors declare no conflicts of interest.

Author Contributions

Q.D., M.J., J.Q., and P.S. contributed equally to this work. Q.D. conceived the idea of the PPM and the potential applications. Q.D. performed the design and simulation for the PPM, PSR, the polarization analyzer, and the polarization stabilizer. M.J. performed the design and simulation for the optical coherent receiver. P.N. performed the design and simulation for the polarization synthesizer. Q.D., M.J., P.S., H.S., Y.T., and Z.T. performed the experiments of the PPM and PRS. M.J., J.Q., H.S., C.J., P.Z., and X.X. performed the experiments of the optical coherent receiver systems. Q.D. and P.S. performed the experiments of the polarization analyzer and stabilizer. P.N. performed the experiments of the polarization synthesizer. Q.D. analyzed the data for the PPM, the PSR, the polarization management applications. M.J. and J.Q. analyzed the optical coherent receiver data. M.J., B.W., B.B., X.Z., and L.L. contributed the SEM analysis and the optical microscope imaging. M.J. and J.S. performed the packaging. Z.Z., X.W., and P.D. supervised this research and provided the financial support. Q.D., M.J., and J.Q. wrote the manuscript. All authors reviewed the manuscript.

Data Availability Statement

The data that support the findings of this study are available from the corresponding author upon reasonable request.

Keywords

optical coherent receiver, polarization management, polarization rotator and splitter, silicon photonics

[1] Z.-Y. Chen, L.-S. Yan, Y. Pan, L. Jiang, A.-L. Yi, W. Pan, B. Luo, *Light: Sci. Appl.* **2016**, *6*, e16207.

[2] H. Hu, F. Da Ros, M. Pu, F. Ye, K. Ingerslev, E. Porto da Silva, M. Nooruzzaman, Y. Amma, Y. Sasaki, T. Mizuno, Y. Miyamoto, L. Ottaviano, E. Semenova, P. Guan, D. Zibar, M. Galili, K. Yvind, T. Morioka, L. K. Oxenløwe, *Nat. Photonics* **2018**, *12*, 469.

[3] A. A. Jørgensen, D. Kong, M. R. Henriksen, F. Klejs, Z. Ye, Ò. B. Helgason, H. E. Hansen, H. Hu, M. Yankov, S. Forchhammer, P. Andrekson, A. Larsson, M. Karlsson, J. Schröder, Y. Sasaki, K. Aikawa, J. W. Thomsen, T. Morioka, M. Galili, V. Torres-Company, L. K. Oxenløwe, *Nat. Photonics* **2022**, *16*, 798.

[4] Z. Zhan, M. Cantono, V. Kamalov, A. Mecozzi, R. Müller, S. Yin, J. C. Castellanos, *Science* **2021**, *371*, 931.

[5] X.-C. Yu, Y. Zhi, S.-J. Tang, B.-B. Li, Q. Gong, C.-W. Qiu, Y.-F. Xiao, *Light: Sci. Appl.* **2018**, *7*, 18003.

[6] S. Zhou, J. Bian, P. Chen, M. Xie, J. Chao, W. Hu, Y. Lu, W. Zhang, *Light: Sci. Appl.* **2022**, *11*, 64.

[7] M. L. Harris, C. S. Adams, S. L. Cornish, I. C. McLeod, E. Tarleton, I. G. Hughes, *Phys. Rev. A* **2006**, *73*, 062509.

[8] L. Tong, X. Huang, P. Wang, L. Ye, M. Peng, L. An, Q. Sun, Y. Zhang, G. Yang, Z. Li, F. Zhong, F. Wang, Y. Wang, M. Motlag, W. Wu, G. J. Cheng, W. Hu, *Nat. Commun.* **2020**, *11*, 2308.

[9] M. Sakamoto, H. T. Nhan, K. Noda, T. Sasaki, M. Tanaka, N. Kawatsuki, H. Ono, *Sci. Rep.* **2022**, *12*, 15268.

[10] H. Shu, L. Chang, Y. Tao, B. Shen, W. Xie, M. Jin, A. Netherton, Z. Tao, X. Zhang, R. Chen, B. Bai, J. Qin, S. Yu, X. Wang, J. E. Bowers, *Nature* **2022**, *605*, 457.

[11] X. Zhang, K. Kwon, J. Henriksson, J. Luo, M. C. Wu, *Nature* **2022**, *603*, 253.

[12] I. Kim, R. J. Martins, J. Jang, T. Badloe, S. Khadir, H.-Y. Jung, H. Kim, J. Kim, P. Genevet, J. Rho, *Nat. Nanotechnol.* **2021**, *16*, 508.

[13] E. Pelucchi, G. Fagas, I. Aharonovich, D. Englund, E. Figueroa, Q. Gong, H. Hannes, J. Liu, C.-Y. Lu, N. Matsuda, J.-W. Pan, F. Schreck, F. Sciarrino, C. Silberhorn, J. Wang, K. D. Jöns, *Nat. Rev. Phys.* **2022**, *4*, 194.

[14] Z. Lin, Y. Lin, H. Li, M. Xu, M. He, W. Ke, H. Tan, Y. Han, Z. Li, D. Wang, X. S. Yao, S. Fu, S. Yu, X. Cai, *Light: Sci. Appl.* **2022**, *11*, 93.

[15] J. Xiang, Z. Tao, X. Li, Y. Zhao, Y. He, X. Guo, Y. Su, *Light: Sci. Appl.* **2022**, *11*, 168.

[16] B. Sun, F. Morozko, P. S. Salter, S. Moser, Z. Pong, R. B. Patel, I. A. Walmsley, M. Wang, A. Hazan, N. Barré, A. Jesacher, J. Fells, C. He, A. Katiyi, Z.-N. Tian, A. Karabchevsky, M. J. Booth, *Light: Sci. Appl.* **2022**, *11*, 214.

[17] Y. Ding, L. Liu, C. Peucheret, H. Ou, *Opt. Express* **2012**, *20*, 20021.

[18] H. Guan, A. Novack, M. Streshinsky, R. Shi, Q. Fang, A. E.-J. Lim, G.-Q. Lo, T. Baehr-Jones, M. Hochberg, *Opt. Express* **2014**, *22*, 2489.

[19] Y. He, Y. Zhang, X. Wang, B. Liu, X. Jiang, C. Qiu, Y. Su, R. Soref, in *2017 Optical Fiber Communications Conf. and Exhibition (OFC)*, IEEE, Piscataway, NJ **2017**, pp. 1–3.

[20] L. Liu, Y. Ding, K. Yvind, J. M. Hvam, *Opt. Lett.* **2011**, *36*, 1059.

[21] L. Liu, Y. Ding, K. Yvind, J. M. Hvam, *Opt. Express* **2011**, *19*, 12646.

[22] Y. Liu, S. Wang, Y. Wang, W. Liu, H. Xie, Y. Yao, Q. Song, X. Zhang, Y. Yu, K. Xu, *Opt. Lett.* **2019**, *44*, 4495.

[23] K. Tan, Y. Huang, G.-Q. Lo, C. Yu, C. Lee, in *Optical Fiber Communication Conf. 2017*, Optica Publishing Group, Washington, D.C **2017**, Th1G.7.

[24] Y. Wang, M. Ma, H. Yun, Z. Lu, X. Wang, N. A. F. Jaeger, L. Chrostowski, *IEEE Photonics J.* **2016**, *8*, 7805709.

[25] K. Yu, L. Wang, W. Wu, Y. Luo, Y. Yu, *Opt. Commun.* **2019**, *431*, 58.

[26] T. Zhang, X. Ke, X. Yin, L. Chen, X. Li, *Sci. Rep.* **2017**, *7*, 12169.

[27] Y. Zhang, Y. He, X. Jiang, B. Liu, C. Qiu, Y. Su, R. A. Soref, *APL Photonics* **2016**, *1*, 091304.

[28] Y. Zhang, Q. Zhu, Y. He, Y. Su, in *Optical Fiber Communication Conf. 2019*, Optica Publishing Group, Washington, D.C **2019**, W1E.4

[29] Y. R. R. Bustamante, G. B. de Farias, H. A. de Andrade, H. E. Hernandez-Figueroa, *Photonics Nanostruct.—Fundam. Appl.* **2021**, *45*, 100921.

[30] D. Chen, D. Chen, M. Liu, Y. Zhang, Y. Zhang, L. Wang, L. Wang, X. Hu, X. Hu, P. Feng, P. Feng, X. Xiao, X. Xiao, S. Yu, *Opt. Express* **2021**, *29*, 10949.

[31] D. Dai, J. E. Bowers, *Opt. Express* **2011**, *19*, 10940.

[32] D. Dai, H. Wu, *Opt. Lett.* **2016**, *41*, 2346.

[33] X. Dai, Q. Lu, W. Guo, in *2021 Optical Fiber Communications Conf. and Exhibition (OFC)*, Optica Publishing Group, Washington, D.C **2021**, Th1A.31.

[34] Y. Ding, H. Ou, C. Peucheret, *Opt. Lett.* **2013**, *38*, 1227.

[35] Y. Ding, H. Ou, F. D. Ros, C. Peucheret, B. Huang, *Opt. Express* **2013**, *21*, 7828.

[36] L. Fang, H.-Z. Luo, X.-P. Cao, S. Zheng, X.-L. Cai, J. Wang, *Optica* **2019**, *6*, 61.

[37] D. Guo, K. Hou, W. Tang, T. Chu, *J. Semicond.* **2019**, *40*, 6.

[38] D. Guo, T. Chu, *OSA Continuum* **2018**, *1*, 841.

[39] W. Liu, J. Liao, Y. Yu, X. Zhang, *APL Photonics* **2021**, *6*, 071302.

[40] W. Liu, J. Liao, H. Cai, Y. Yu, X. Zhang, *J. Lightwave Technol.* **2022**, *40*, 3794.

[41] M. Ma, A. H. K. Park, Y. Wang, H. Shoman, F. Zhang, N. A. F. Jaeger, L. Chrostowski, *Opt. Express* **2019**, *27*, 17581.

[42] M. Ma, H. Shoman, K. Tang, S. Shekhar, N. A. F. Jaeger, L. Chrostowski, *Opt. Express* **2020**, *28*, 1885.

[43] Y. Ma, Y. Liu, H. Guan, A. Gazman, Q. Li, R. Ding, Y. Li, K. Bergman, T. Baehr-Jones, M. Hochberg, *Opt. Express* **2015**, *23*, 16052.

[44] A. Melikyan, K. Kim, N. Fontaine, S. Chandrasekhar, Y.-K. Chen, P. Dong, *Opt. Express* **2018**, *26*, 18523.

[45] A. Melikyan, P. Dong, *APL Photonics* **2019**, *4*, 030803.

[46] A. Rostamian, J. Guo, S. Chakravarty, H. Yan, C. J. Chung, E. Heidari, R. T. Chen, *IEEE Photonics Technol. Lett.* **2019**, *31*, 401.

[47] W. D. Sacher, T. Barwicz, B. J. F. Taylor, J. K. S. Poon, *Opt. Express* **2014**, *22*, 3777.

[48] W. D. Sacher, Y. Huang, L. Ding, T. Barwicz, J. C. Mikkelsen, B. J. F. Taylor, G.-Q. Lo, J. K. S. Poon, *Opt. Express* **2014**, *22*, 11167.

[49] C. Sun, Y. Yu, G. Chen, X. Zhang, *IEEE Photonics Technol. Lett.* **2016**, *28*, 2253.

[50] W. Wu, Y. Yu, W. Liu, X. Zhang, *Nanophotonics* **2019**, *8*, 467.

[51] H. Xu, Y. Shi, *Opt. Express* **2017**, *25*, 18485.

[52] C. Yuan, J. Dai, H. Jia, J. Ding, L. Zhang, X. Fu, L. Yang, *J. Semicond.* **2018**, *39*, 124008.

[53] W. Zhao, R. Liu, Y. Peng, X. Yi, H. Chen, D. Dai, *Nanophotonics* **2022**, *11*, 2293.

[54] Y. Zhao, C. Qiu, A. Wu, H. Huang, J. Li, Z. Sheng, W. Li, X. Wang, F. Gan, *IEEE Photonics J.* **2019**, *11*, 6600310.

[55] W. Chang, S. Xu, M. Cheng, D. Liu, M. Zhang, *Opt. Express* **2020**, *28*, 28343.

[56] N. Lebbe, A. Glière, K. Hassan, *Opt. Lett.* **2019**, *44*, 1960.

[57] A. Majumder, B. Shen, R. Polson, R. Menon, *Opt. Express* **2017**, *25*, 19721.

[58] Z. Yu, H. Cui, X. Sun, *Opt. Lett.* **2017**, *42*, 3093.

[59] L. Gao, Y. Huo, J. S. Harris, Z. Zhou, *IEEE Photonics Technol. Lett.* **2013**, *25*, 2081.

[60] L. Gao, Y. Huo, K. Zang, S. Paik, Y. Chen, J. S. Harris, Z. Zhou, *Sci. Rep.* **2015**, *5*, 15794.

[61] A. V. Velasco, M. L. Calvo, P. Cheben, A. Ortega-Moñux, J. H. Schmid, C. A. Ramos, Í. M. Fernandez, J. Lapointe, M. Vachon, S. Janz, D.-X. Xu, *Opt. Lett.* **2012**, *37*, 365.

[62] D. Vermeulen, S. Selvaraja, P. Verheyen, P. Absil, W. Bogaerts, D. Van Thourhout, G. Roelkens, S. Member, D. V. Thourhout, *IEEE Photonics Technol. Lett.* **2012**, *24*, 482.

[63] Z. C. Wang, D. X. Dai, *J. Opt. Soc. Am. B* **2008**, *25*, 747.

[64] H. Xu, Y. Shi, *Opt. Express* **2019**, *27*, 5588.

[65] H. Zhou, C. Li, A. L. Eujin, L. Jia, M. Yu, G. Lo, *Opt. Express* **2015**, *23*, 6815.

[66] T. Barwicz, M. R. Watts, M. A. Popovi, P. T. Rakich, L. Socci, F. X. Kärtner, E. P. Ippen, H. I. Smith, *Nat. Photonics* **2007**, *1*, 57.

[67] C. Alonso-Ramos, R. Halir, A. Ortega-Moñux, P. Cheben, L. Vivien, Í. Molina-Fernández, D. Marris-Morini, S. Janz, D.-X. Xu, J. Schmid, *Opt. Lett.* **2012**, *37*, 3534.

[68] J. D. Sarmiento-Merenguel, R. Halir, X. Le Roux, C. Alonso-Ramos, L. Vivien, P. Cheben, E. Durán-Valdeiglesias, I. Molina-Fernández, D. Marris-Morini, D. X. Xu, J. H. Schmid, S. Janz, A. Ortega-Moñux, *Optica* **2015**, *2*, 1019.

[69] Q. Deng, Q. Yan, L. Liu, X. Li, J. Michel, Z. Zhou, *Opt. Express* **2016**, *24*, 7347.

[70] H. Xu, Y. Shi, *IEEE Photonics Technol. Lett.* **2018**, *30*, 169.

[71] Q. Deng, L. Liu, X. Li, Z. Zhou, *Opt. Lett.* **2014**, *39*, 5590.

[72] T. Gui, X. Wang, M. Tang, Y. Yu, Y. Lu, L. Li, *J. Lightwave Technol.* **2021**, *39*, 1231.

[73] M. He, M. Xu, Y. Ren, J. Jian, Z. Ruan, Y. Xu, S. Gao, S. Sun, X. Wen, L. Zhou, L. Liu, C. Guo, H. Chen, S. Yu, L. Liu, X. Cai, *Nat. Photonics* **2019**, *13*, 359.

[74] M. R. Watts, J. Sun, C. DeRose, D. C. Trotter, R. W. Young, G. N. Nielson, *Opt. Lett.* **2013**, *38*, 733.

[75] C. Ju, N. Liu, C. Li, Z. Wang, *Opt. Fiber Technol.* **2020**, *58*, 102255.

[76] F. Gardner, *IEEE Trans. Commun.* **1986**, *34*, 423.

[77] C. Liu, J. Pan, T. Detwiler, A. Stark, Y.-T. Hsueh, G.-K. Chang, S. E. Ralph, *Opt. Express* **2013**, *21*, 8342.

[78] Q. Zhang, C. Shu, *J. Lightwave Technol.* **2021**, *39*, 1364.

[79] R. Schmogrow, B. Nebendahl, M. Winter, A. Josten, D. Hillerkuss, S. Koenig, J. Meyer, M. Dreschmann, M. Huebner, C. Koos, J. Becker, W. Freude, J. Leuthold, *IEEE Photonics Technol. Lett.* **2012**, *24*, 61.